

Stochastic models of compliant spine arrays for rough surface grasping

The International Journal of
Robotics Research
2018, Vol. 37(7) 669–687
© The Author(s) 2018
Reprints and permissions:
sagepub.co.uk/journalsPermissions.nav
DOI: 10.1177/0278364918778350
journals.sagepub.com/home/ijr



Hao Jiang* , Shiquan Wang*  and Mark R Cutkosky

Abstract

This paper presents models of arrays of compliantly supported spines that attach to rough surfaces. The applications include climbing and perching robots. Surfaces are characterized in terms of asperity distributions, which lead to stochastic models of spine force capabilities over a range of loading directions. Models cover unidirectional spine arrays and pairs of opposed arrays that withstand normal forces pulling away from a surface. Experiments on a variety of surfaces confirm the predicted behavior. For opposed spine arrays, the overall load capability also depends on the preloading strategy for applying internal forces. Insights from the analysis guide the design of spine array mechanisms to allow, for example, a small aerial platform to attach to walls and ceilings.

Keywords

Spines, grasping, adhesion modeling, gripper design

1. Introduction

Over the last decade there has been increasing interest in solutions that allow robots to attach to surfaces outdoors. Applications include robots that climb on brick or concrete walls and micro air vehicles that can land and perch on roofs, walls and inverted surfaces such as the underside of a bridge (Figure 1). Among the various technologies proposed, micro-spines have a number of advantages: they work on many rough surfaces including stucco, brick, stone, and concrete; they are relatively unaffected by surface moisture or dirt; they do not require power; and they require very little effort to engage and disengage. Demonstrations of spines include climbing robots (Asbeck et al., 2006; Daltorio et al., 2009; Lam and Xu, 2012; Lee and Fearing, 2015; Liu et al., 2015; Lynch et al., 2012; Parness et al., 2015; Pope and Cutkosky, 2016; Sintov et al., 2011; Spenko et al., 2008; Wang et al., 2016; Xu et al., 2017), ying robots that land on walls and similar surfaces (Desbiens et al., 2011; Jiang et al., 2014; Kovac et al., 2009; Pope et al., 2017; Roderick et al., 2017) and proposed space robots that can attach to asteroids or rocky features on planets (Parness, 2011; Parness et al., 2013).

Modeling of micro-spine attachment for robotics dates back to 2006 (Asbeck et al., 2006) and is inspired by the analysis of the spines of insects that cling to rough surfaces (Dai et al., 2002). Micro-spines are small hooks or spines, with a tip radius of the order $10\ \mu\text{m}$ when sharp, that engage small asperities (bumps or pits) on a rough surface.

Arrays of micro-spines can support large loads (up to 5 N per spine on concrete surfaces) primarily in shear but also with a small normal component pulling away from a surface. However, the ability to support loads is also stochastic. First, a spine must engage a suitable asperity on the surface, which depends on the spatial distribution of asperities and on the distribution of their surface profiles. Once engaged, the ability to support a force is also stochastic, depending on details of the spine/asperity contact geometry, the asperity strength (which is uncertain for brittle and cementitious materials (Mombor, 2004)) and the loading direction.

Previous work has modeled the spatial distribution of asperities on a surface and considered the relationship between asperity size (related to surface roughness) and the forces that a spine can exert (Asbeck et al., 2006). Additional work has modeled individual spines and suspensions to determine parameters that promote effective engagement (Asbeck and Cutkosky, 2012). Other work has presented the design of systems that harness groups of spines to create surface-gripping mechanisms that support loads from a wide range of directions (Jiang et al., 2014; Parness, 2011; Parness et al., 2013).

Department of Mechanical Engineering, Stanford University, Stanford, CA, USA

Corresponding author:

Hao Jiang, Biomimetic and Dexterous Manipulation Lab, 418 Panama Mall, Building 02-660, Room 132, Stanford, CA 94305, USA.
Email: jjianghao@stanford.edu

*These authors contributed equally.

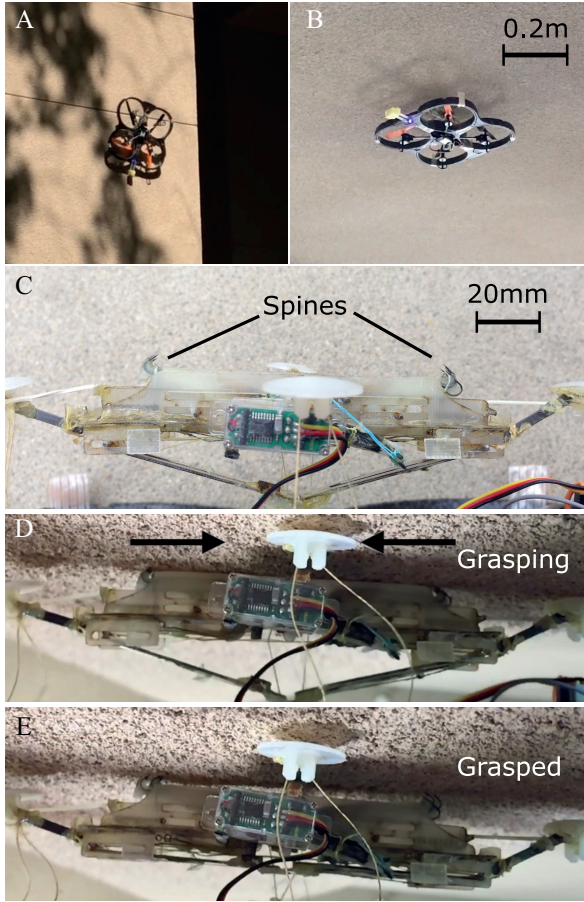


Fig. 1. A radio-controlled quadrotor perches on vertical and inverted rough surfaces using an opposed micro-spine mechanism on the top for adhesion: (A) quadrotor perching on a vertical concrete wall; (B) quadrotor perching on an overhanging concrete surface; (C)–(E) surface grasping sequence.

The work presented here presents a stochastic model of spine/asperity interaction that can be used to predict the expected forces from groups of spines and guide the design of mechanisms for perching and climbing robots. Specific contributions are:

- models, confirmed with experiments on three different surfaces, of asperity distributions and corresponding distributions of expected forces for spines loaded in various directions;
- design guidelines for mechanisms and loading strategies for opposed arrays of spines that will provide the best expected performance for a given range of loading directions;
- the design of an opposed micro-spine mechanism that enables quadrotors to perch reliably on rough vertical and inverted surfaces.

Section 2 introduces the current micro-spine design, which builds upon previous work, as well as surface property measurement and modeling. Section 3 presents a model

of spine/asperity interaction that accounts for the probability that some spines will fail early during the loading process and then reattach, contributing significantly to the overall performance. Section 4 extends the analysis to opposed micro-spines. The effects of different preload strategies are taken into account for omnidirectional adhesion. Section 5 demonstrates a typical application and the design of a mechanism that allows a quadrotor to perch on walls and ceilings. Section 6 concludes this work and discusses future directions.

2. Spine theory

2.1. Compliantly supported micro-spines

As shown in previous work (Asbeck et al., 2006), a compliantly supported micro-spine has a moderately stiff flexure along the shear direction for loading and a very soft flexure in the normal direction for preloading. A compliant stalk model has been developed to describe the behaviors of such micro-spines in climbing applications (Asbeck and Cutkosky, 2012). Here, we adapt the design insights from previous work and modify the configuration for grasping applications.

Figure 2 compares the micro-spine configuration for grasping (D) with the previous, longer configuration used for climbing (C). Let d_{unit} be the unit length of a micro-spine mechanism, as shown in (A). There is also typically an offset, h_{mis} , which corresponds to how close the point of application of the external load can be to the surface. The spine force is decomposed into components, F_n and F_s , normal and tangential to the surface, respectively. In addition, depending on the load application point and angle, there may be normal and tangential (i.e. frictional) forces, F_c and F_f , where the rear of the spine mechanism contacts a surface. The point where F_c and F_f act changes very slightly due to spine hook deflection on most asperities. The shape of the spine body ensures an almost fixed rear contact point. Taking a force and moment balance, the limiting case occurs as $F_c \rightarrow 0$ and

$$\frac{F_n}{F_s} = \frac{h_{mis}}{d_{unit}} = \tan \theta_m \quad (1)$$

As shown in Figure 2(B), there is a range of force directions limited by θ_{th} that the spine/asperity contact can sustain without slipping. Depending on d_{unit} , θ_m may be smaller than θ_{th} . This implies that if a micro-spine catches an asperity and can be loaded in the shear direction, then it can also sustain a load up to θ_m with the same shear force component, without danger of slipping.

For many grasping applications, micro-spines travel in shear first to find an asperity to latch onto before being loaded away from the surface. Given that $F_s \gg F_f$, the loading angle will be approximately θ_m . The shorter d_{unit} is, the

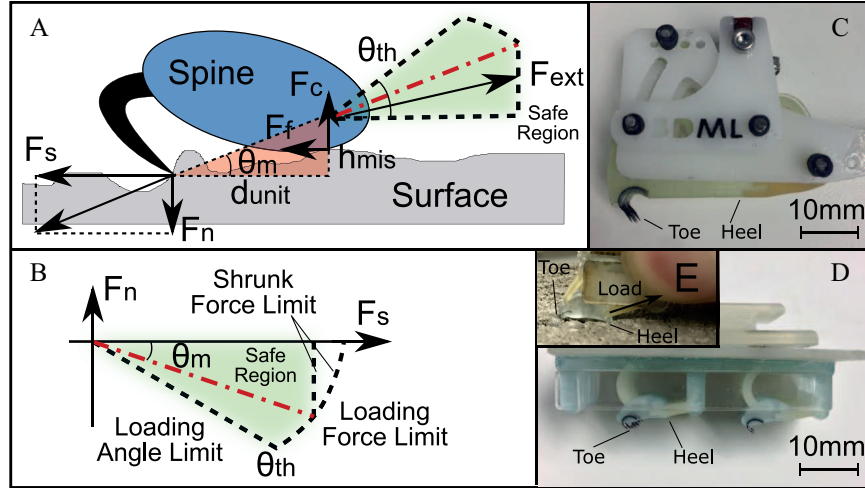


Fig. 2. Comparison of original and compact micro-spine mechanisms: (A) compliantly supported micro-spine and force balance; (B) reduction in safe loading region for $\theta_m < \theta_{th}$; (C) original mechanism for climbing, with long d_{unit} ; (D) new design with short d_{unit} ; (E) new design with a load away from the surface, only toe and heel contacting, as in (A).

higher the loading angle can be guaranteed upon engagement. By traveling along the surface, the micro-spine automatically filters out bad asperities that cannot sustain a loading angle up to θ_m . After the spines are loaded away from a surface, there is very little chance of re-engagement. Therefore, it is important to make sure each spine only engages with a good asperity. Note that the external load limit at a low loading angle shrinks compared to the natural load limit of the asperity (Figure 2(B)). In practice, if $\theta_m < 25^\circ$ the shrinkage of the potential safe region for spine/asperity contacts is within 10%. Therefore, by making d_{unit} shorter than in the original climbing case, we enlarge the range of feasible external loading angles without greatly decreasing the number of usable asperities. This design modification is desirable for grasping applications. Note that for climbing applications where shear loading is dominant, the stalk model in Asbeck and Cutkosky (2012) well guides the design toward a long d_{unit} such that the heel of the spine does not contact the surface to prevent limit curve shrinkage in Figure 2(B).

2.2. Surface properties

There are three surface properties that affect micro-spine performance: the asperity *spatial* distribution, the spine-asperity *contact strength* distribution, and the asperity *angle* distribution. The spatial distribution reflects the probability of spine-asperity engagement for a given length of travel along a surface. The contact strength distribution determines the amount of adhesion a spine/asperity pair can take before either the asperity breaks or the micro-spine slips off. The asperity angle distribution affects the loading angle limit. The asperity angle distribution has been measured and characterized for stone, concrete, and similar surfaces in previous work (Asbeck et al., 2006). In general, it was

found that asperity density decreases with desired asperity steepness (which allows a higher loading angle). The decreasing trend can be approximated with a polynomial fit. In the following sections we examine the asperity spatial and contact strength distributions in more detail.

2.2.1. Asperity spatial distribution With the assumption that asperities are randomly located on surfaces, we can model the asperity occurrence as a spatial Poisson process with a mean interval distance. Thus, the interval distance between adjacent asperities is described by an exponential distribution. It can also be shown that, starting at a random place on a surface, the probability of the traveling distance of a micro-spine before catching the next asperity follows the same exponential distribution as the asperity interval distance. The derivation is given in Appendix A.

In addition, for a variety of surfaces, given the fact that micro-spine tips are very sharp (tip radius on the order of 10 μm), asperities have finite lengths such that a micro-spine can catch at any point on an asperity. Thus, on this finite length, one can regard the entire asperity as an infinite number of small asperities with zero interval distance. In other words, a spine has a non-zero probability to engage with an asperity upon an initial contact. Combining the real interval distance between asperities and the finite length of asperities, we model the asperity distribution as a two-phase distribution with a parameter α to balance the probability concerning how far asperities are spaced apart (exponential term) and how long an asperity is (initial term):

$$\begin{aligned} p(\alpha, \lambda; x) &= \alpha p_{exp} + (1 - \alpha)p_{init} \\ &= \alpha \lambda e^{-\lambda x} + (1 - \alpha)\delta(x), \quad x > 0 \end{aligned} \quad (2)$$

where x is a random variable describing the interval distance between adjacent asperities, λ is the average number

of asperities per unit length on a surface, $1 - \alpha$ is the probability of immediate engagement when a micro-spine arbitrarily lands on a surface, and $\delta(x)$ is the impulse function that can be treated as an extreme case of exponential distribution with λ equal to infinity. As later used to model the micro-spine adhesion on different surfaces, the exponential term mainly affects the engagement of soft micro-spines with large travel and long flexure stretch, and the $\delta(x)$ special initial term mainly affects the performance of stiff micro-spines with little travel and short flexure extension.

Experiments were conducted with a single micro-spine mechanism of $d_{unit} = 8$ mm starting at an arbitrary position on a surface and dragged along the surface. The traveling distance between the starting point and the first asperity caught was measured with a machinist's ruler. The comparison between the model and the experiment on three different surfaces (concrete block, roofing shingle, 80-grit sand paper) is shown in Figure 3. The first two surfaces are likely to occur in applications such as unmanned aerial vehicle (UAV) perching. The 80-grit sandpaper is chosen as a comparable surface with a well-defined asperity size. The roofing shingle and sandpaper have convex asperities, which can promote sideways slipping of spines. In contrast, the cast concrete block has primarily concave asperities that support spines stably, so that the limiting factor is usually the spine strength. There are 150 measurement trials for each surface. Here α is computed with the probability of non-zero travel before engagement, and λ is obtained from the mean traveling distance excluding zero-travel trials. The model and results of experiments match reasonably closely, with higher variation at low interval distances. This is because the distance measurement has a fixed, 1 mm resolution, and the measurement is slightly less accurate when the distance value is low. However, as shown in Section 3, the model is good enough for further adhesion analysis.

2.2.2. Asperity strength distribution As noted in Asbeck et al. (2006), spine/asperity contact strength is limited by (i) the strength of the asperity on the surface and (ii) the strength of the spine, which can bend and slip off the asperity. Depending on the surface, the spine and asperity strength distributions can overlap.

Experiments were conducted by pulling a single spine quasi-statically along concrete, roofing shingle, and sandpaper surfaces until the spine engaged. Forces were then increased until either the spine/asperity contact failed or a limit of 3 N was reached, to prevent damaging the spines. Forces were measured with a force gauge (Mark-10 Series 4). Forces below 0.5 N were difficult to measure accurately; therefore, the probability of contact strength less than 0.5 N is neglected. Such weak asperities are also of low practical interest. The experimental data of the cumulative probability associated with each load from 0.5–3.0 N are shown in Figure 4. As discussed in Appendix B, 150 measurements are sufficient for the data to converge.

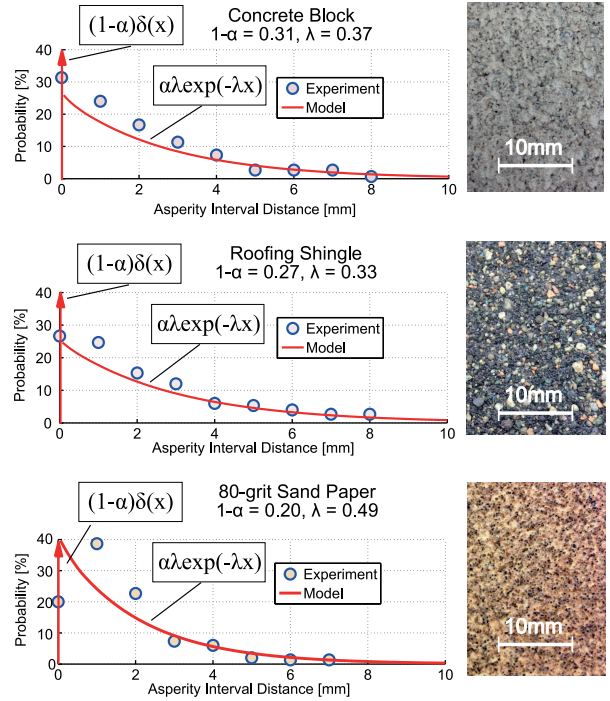


Fig. 3. Comparison of two-phase model and experimental asperity spatial distributions on three surfaces. The red arrow shows the δ function scaled with $(1 - \alpha)$; the red curve shows the exponential term. Empirical data obtained by dragging a compliantly supported spine and measuring distance to first engagement with a machinist's ruler (accuracy ≈ 1 mm).

The data do not obviously match a standard probability function. Therefore, we obtain $g(f)$ directly from the raw measurements. Let η be the cumulative probability of an asperity strength higher than 3 N. For concrete and roofing shingle, η is large enough that a straight line can be used to approximate the cumulative distribution, which corresponds to a uniform distribution in the probability density function of asperity strength. For sandpaper, for which η is small, the error of using a straight line approximation is larger. However, for such comparatively weak surfaces it may be preferable to stop at a limit below 3 N, which improves the straight-line approximation. The cumulative probability of the asperity strength larger than a specific force can be described as follows:

$$Pr(F) = \begin{cases} 1 & \text{if } F \leq 0.5 \\ \eta + \int_F^3 g(f) & \text{if } 0.5 < F < 3 \\ \eta & \text{if } F \geq 3 \end{cases} \quad (3)$$

where $g(f)$ is the probability density function for spine-asperity contact strength between 0.5 and 3 N.

2.2.3. Practical methods for surface characterization. Although the aforementioned surface properties can be measured by dragging a compliant micro-spine across a surface and recording the results, it is not practical to measure

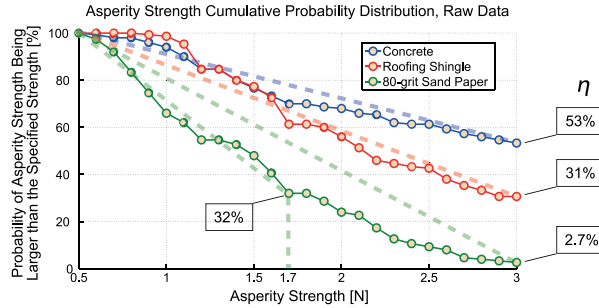


Fig. 4. Experimental data of the asperity strength distribution (cumulative probability) on three surfaces: fine concrete, roofing shingle, and 80-grit sandpaper. Each surface has 150 measurements. Each data point indicates the probability of a spine/asperity contact strength larger than this force. Straight dashed lines indicate using uniform distributions as approximations.

every surface using a prepared spine for several hundred trials before applying loads. However, if a robotic end-effector consisting of a large group of spines is equipped with displacement and force sensors that can measure the traveling distance and the total force, then the instantaneous stiffness of the spine group can be calculated. This stiffness will be proportional to the number of engaged spines at any travel distance. From these measurements, the maximum adhesion of the failed spines can also be computed. As the force ramps up, the magnitude of any transient drops in force will be an indication of the corresponding maximum force on a spine. Thus, in practical use, it is feasible for a robot to know the asperity distributions by using its instrumented spine-array feet to scrape along a surface for only a few trials. For the purposes of force prediction and mechanism design in this paper, we build upon the surface properties measured by single spines as presented above.

3. Unidirectional spine tile

In this section, we consider the performance of an array of spines mounted to a tile. Based on considerations from the previous section, the spines here are intended for use with an initial shear preload and accordingly have a short unit length, which leads to a denser packing than in previous work (Asbeck et al., 2006).

3.1. Shear adhesion evaluation

A schematic view of a spine tile is shown in Figure 5. The shear force at a given tile travel depends on the asperity spatial distribution, the spine/asperity contact strength distribution, the travel of the spine tile base, the spine stiffness, and the number of spines. The force per unit area, or shear stress, also depends on design parameters including the unit length and flexure length. We first use a simple model in which spines do not have the chance to re-engage if they slip off an asperity as the tile travels. We then extend the model to consider possible re-engagement.

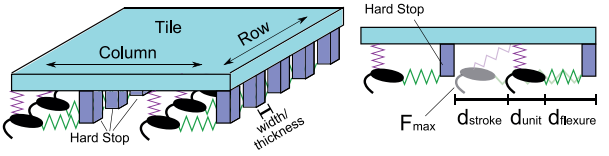


Fig. 5. Schematic diagram of a tile of compliantly supported micro-spines. Here d_{unit} is the length of the spine body, which consists of a spine hook embedded in a plastic part, d_{stroke} is the length of allowed deflection of a spine flexure before the spine hits its hard stop, the spine force reaches its maximum F_{max} at the end of the deflection, and $d_{flexure}$ is the original flexure length.

Next, we present two models with different levels of accuracy to describe the shear adhesion of a group of spines. The simplified model considers the process of spine traveling, engaging, and slipping as a one-time calculation and does not consider spine re-engagement after failing. The recursive model divides the process into discrete displacement segments and calculates the total force with recursion. Spine re-engagement is considered.

3.1.1. Simplified model Because the asperity spatial distribution and strength distributions are independent, the probability of a micro-spine catching an asperity and holding a certain force is a multiplication of the two distributions. The loading process can be described by a simple decision tree, as shown in Figure 6. The shear stress of a group of independent micro-spines can be calculated as follows:

$$E[\sigma] = \frac{\int_0^{d_{stroke}} p(\alpha, \lambda; x) F(x) Pr(F(x)) dx}{(d_{unit} + d_{flexure} + d_{stroke}) w} \quad (4)$$

$$\begin{aligned} F(x) &= K(d_{stroke} - x) \\ &= \frac{F_{max}}{d_{stroke}} (d_{stroke} - x) \end{aligned} \quad (5)$$

where $E[\sigma]$ is the expected stress at full travel, $d_{flexure}$ is the flexure length of each unit, d_{stroke} is the maximum travel of the tile base, as well as the interval spacing between spine rows, $p(\alpha, \lambda; x)$ is the probability density of engagement with travel x , $F(x)$ is the force of a single spine free traveling x to engage and being loaded to the maximum traveling distance, $Pr(F(x))$ is the cumulative probability of an asperity stronger than $F(x)$, w is the width of a single micro-spine in the direction perpendicular to travel, K is the spine stiffness, and F_{max} is the force of a spine at the maximum stretch (d_{stroke}). Note that physically the spine can possibly take larger forces after hitting the hard stop, but for the analyses and experiments in this paper, we stop the loading at full stretch to protect the spines from damage. Similarly, the standard deviation of the stress can be calculated based on the two asperity distributions.

In experiments, five tiles were manufactured with different stroke lengths, d_{stroke} , ranging from 1.5 to 8.5 mm. All tiles had 20 micro-spines and the same unit length $d_{unit} = 8$ mm and maximum spine force, $F_{max} = 3$ N. Each tile was

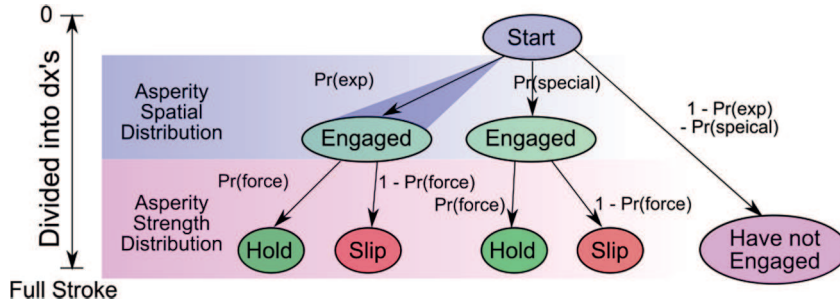


Fig. 6. Schematic of the loading process using a decision tree.

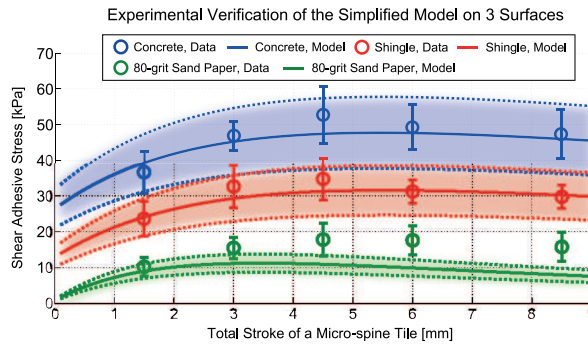


Fig. 7. Empirical verification of the simplified model for tiles with 20 spines and various designed values of d_{stroke} . Blue data points and curve are for concrete, red is for roofing shingle and green for 8 grit sandpaper. Shaded regions show one standard deviation of the model; error bars show one standard deviation for 20 trials for each stroke length and material.

placed arbitrarily on a concrete, roofing shingle or 80 grit sandpaper surface and loaded in shear to full stroke. The corresponding results for shear stress as a function of d_{stroke} are shown in Figure 7 and compared with the model. Note that different data points correspond to different tiles of spines loaded to full stroke instead of the same tile loaded with sequential strokes. The shaded regions show one standard deviation for the stochastic model. The discrete points and error bars are the mean and one standard deviation of the measured stress. Each data point corresponds to 20 trials. Without the consideration of re-engagement, the simplified model captures the shear performance well on the concrete and roofing shingle surfaces, where asperities are reasonably strong. However, on sandpaper, because the asperities can sustain 3 N with only 2.7% probability, many initially engaged spines cannot hold until full stroke, and spine slippage and re-engagement contribute significantly to the force.

It can be seen from Figure 7 that after d_{stroke} reaches a certain level, e.g. 4 mm, the adhesive stress is not very sensitive to this design parameter, mainly due to the trade-off between load-sharing and spine density. However, this threshold may change based on different surface properties as shown in Figure 14.

3.1.2. Recursive model The limitation of the simplified model can be rectified by considering the possibility of spine re-engagement with a recursive model. The entire loading process along the stroke can be described as a Markov decision process (MDP), as shown in Figure 8. The total stroke can be discretized into several small strokes ΔL . For each stroke increment ΔL , there are three possibilities: (1) if the micro-spine has been able to catch and hold onto an asperity, it has a certain probability to continue to hold during the next increment; (2) if the micro-spine previously engaged with an asperity and then fails to hold, it restarts the engagement cycle; (3) if a spine did not catch any asperity, it is unlikely to immediately engage with an asperity at the beginning of the next cycle, thus there is no initial term for the asperity spatial distribution for this case. For each ΔL , the probability integration has a resolution of dx .

Here, we assume each spine is independent and do not consider the effect of load redistribution when a spine fails. That is, we neglect the effect that the forces of failed spines are taken by the remaining engaged spines during dynamic loading. Instead, we focus on the load-travel relationship and assume the spine tile's travel is controlled during loading. Models and experiments are all established and conducted under this assumption. Considering load redistribution for spine failure will require considering spines' interdependency and constructing multiple interconnected MDPs, which will substantially increase computation. The resulting spine failure probability will be somewhat higher, with less total load capability and larger variation. This will be studied in future work.

The upper plot in Figure 9 shows a comparison of a three-layer recursive model with the simplified model for the case of 80 grit sandpaper. The recursive model provides a better fit. The lower plot shows further that with additional layers, the root-mean-square (RMS) error continues to reduce slightly. Unfortunately, the computational complexity of the MDP grows exponentially along with finer discretization of the stroke. For example, where the simplified model takes approximately 1 second to compute, a four-layer model takes over an hour.

Further error analysis between the simplified model and a three-layer recursive model is demonstrated across different surface properties described by the three variables in

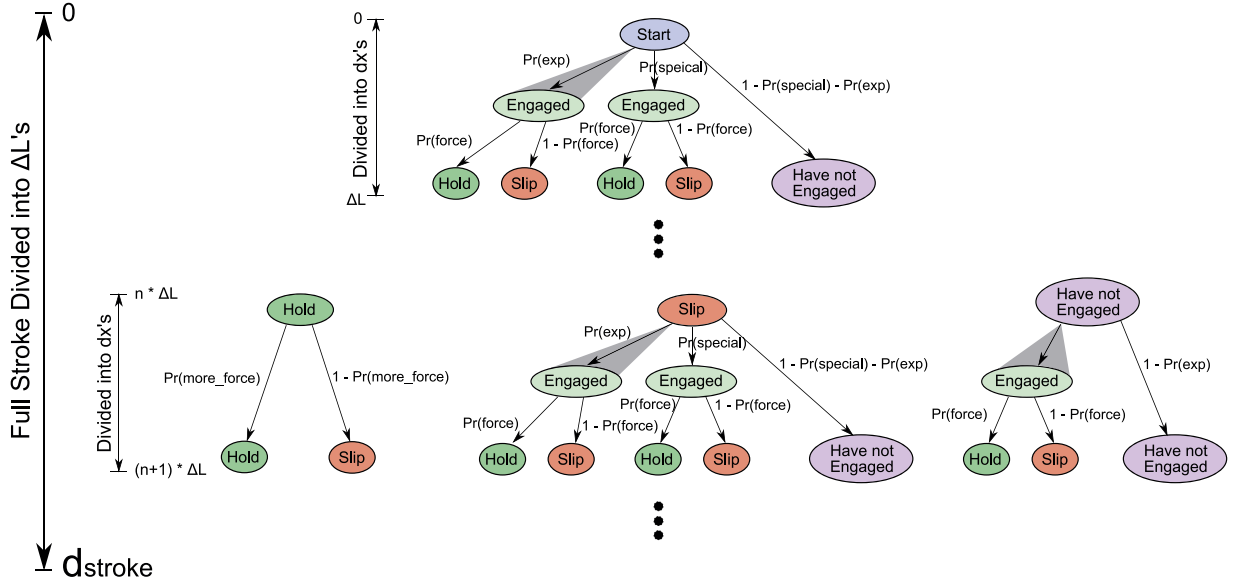


Fig. 8. Illustration of the loading process in the complete model using a recursive MDP.

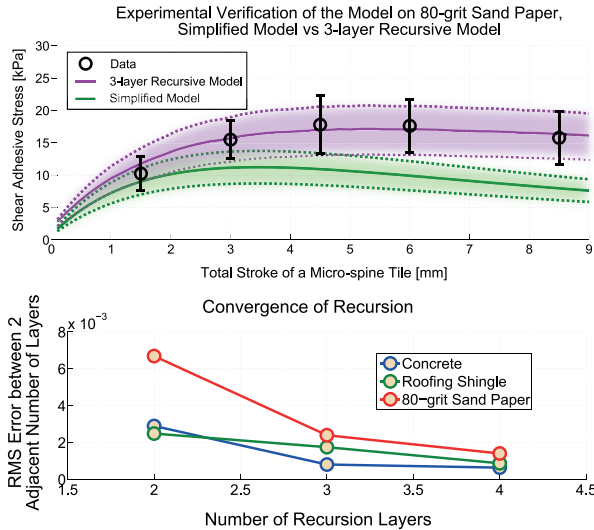


Fig. 9. Comparing the simplified model and recursive model: for weak surfaces such as sandpaper, the recursive model captures the experiment better. The predicted stress converges as the number of recursive layers increases.

Figure 10. For this comparison, we assume a uniform asperity strength distribution. As seen earlier, this is a reasonably good approximation for strong surfaces such as concrete but over-predicts spine forces on weak surfaces (Figure 4). This assumption leads to slight underestimation of model errors on weak surfaces. For the comparison in Figure 10 the spine unit length is fixed at 8 mm; the total stroke is 6 mm, and the maximum single spine force is 2.5 N. The error in the simplified model is often within 10% except for the limiting case of surfaces having a high density of weak asperities; rough plaster or adobe could be examples of such a surface. On such surfaces, it is desirable to not load the spines

to a high force, but rather stop loading in the middle of the stroke. Alternatively one can use a design with a dense spine array to take advantage of the high asperity density and a small maximum force on each spine. More generally, it is reasonable to use the simplified model for further analysis, as it is fast and captures the adhesion performance for most surfaces that are likely to be encountered in practical applications.

3.2. Two-dimensional loading evaluation

The combined tangential/normal loading behavior of a compliant spine tile is similar to the shear loading case except that (i) each spine is now also constrained by its individual loading angle limit and (ii) as spines are loaded increasingly away from the surface they are less likely to re-engage with new asperities. To ensure that most spines are not overloaded we impose tile displacement limits. The shear displacement limit is determined by the distance between spines (Figure 5(A)). The displacement limit in the normal direction is less straightforward because different spines in an array will have different loading angles and force limits. We implement an empirical normal displacement limit for the tile to control the overall loading angle.

We follow a loading trajectory as shown in Figure 11 in which the tile is first preloaded in shear and then pulled away at some angle. During the preload phase, each spine follows the process described in the previous section and summarized in Figure 11. During the loading phase, the probability of spines re-engaging decreases with increasing loading angle because spines are lifted away from the surface, becoming negligible for $\phi > 10^\circ$. Details of the modified probability calculation are given in Appendix C. Note that due to the preload phase, the direction of the tile

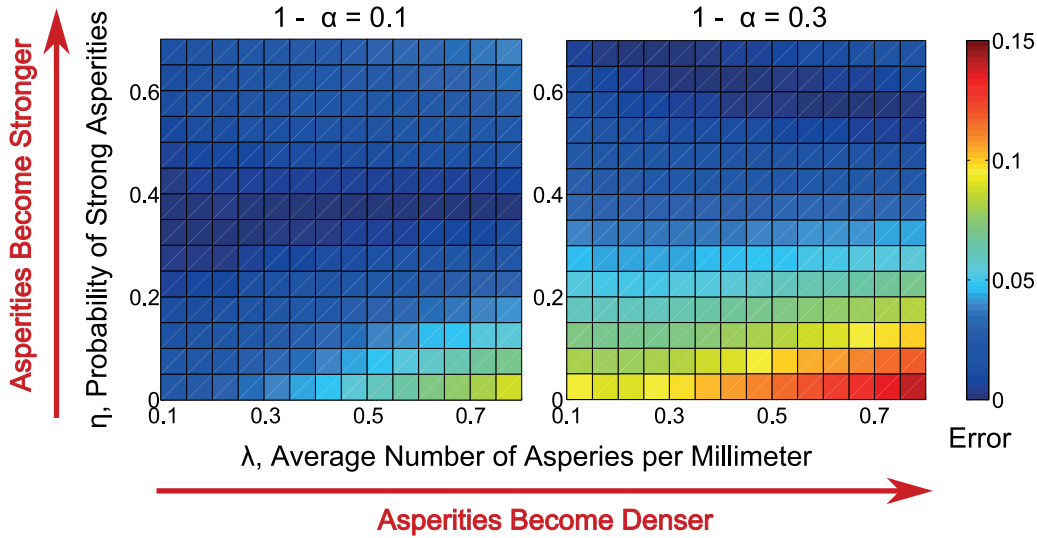


Fig. 10. Comparing the simplified and three-layer recursive models across surface properties ($d_{unit} = 8$ mm, $d_{stroke} = 6$ mm, $F_{max} = 2.5$ N). For most cases, the simplified model captures the performance well.

stroke can be slightly different from the final loading angle (Figure 5 B).

Although individual spine rotation has been cited as a major influence in spine force evaluation (Asbeck and Cutkosky, 2012), we take advantage of a small d_{unit} for an enlarged θ_m such that the majority of the spines are not subject to rotation during shear-normal loading. Note that as long as the tile is loaded away from the surface, it is always possible to have a few spines that engage very late to exceed θ_m . These spines are bounded by θ_{th} and do not have big contributions. Here θ_{th} is stochastic for different asperities, so for simplicity, we choose a fixed, empirically measured, tile-level θ_{th} , and then we assume the force limit for θ_m and θ_{th} is the same, meaning a circular arc from θ_m to θ_{th} in the single spine limit curve in Figure 2(B).

Experiments were conducted with a tile of 20 spines on a concrete surface. The spines had the following parameters: $d_{unit} = 8$ mm, $d_{stroke} = 6$ mm, $F_{max} = 2$ N. The tile was preloaded to one-third of d_{stroke} and then pulled at various angles until reaching either the shear displacement limit (at d_{stroke}) or the normal displacement limit, at $z = 2.54$ mm. Based on measurements of the excursions of spines in the normal direction, the average asperity height was taken as 1 mm. An ATI Gamma SI-130-10 force sensor beneath the surface measured the external load.

Figure 12 shows a comparison of the empirical and predicted forces in the shear and normal directions. One hundred data points were taken for various loading angles and were binned and averaged within every 2° angular range. Error bars indicate one standard deviation along the force vectors. The standard deviation is large when approaching the loading angle limit because this angle will vary for different asperities and the spines become prone to slippage with minor variations in loading. In practical cases, it is unwise to load at angles beyond θ_m , the geometric loading

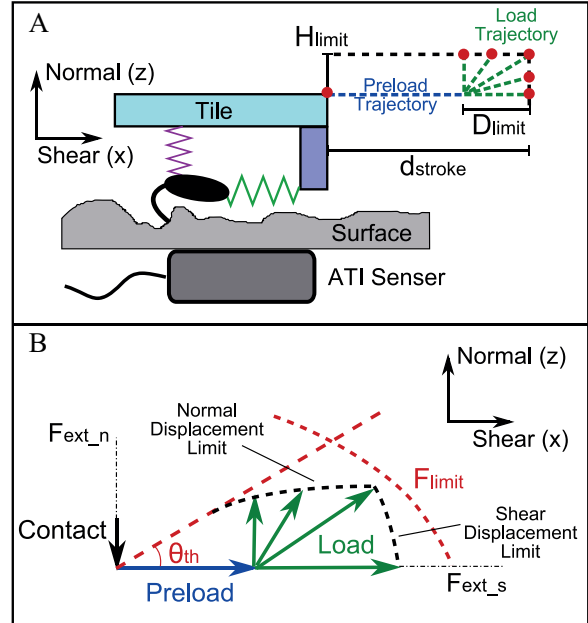


Fig. 11. Illustration of the preloading and loading trajectory for spine tile two-dimensional adhesion evaluation. (A) The experimental setup and the loading trajectory. (B) Illustration of the resulting force vectors at full stroke.

angle limit associated with d_{unit} . The blue solid line shows the modeled mean adhesion, and the blue shaded region shows one standard deviation in the statistical model. The four marked black dots represent transitions among constraints. Proceeding in clockwise (right to left) direction, the first transition occurs when spines can no longer re-engage after slipping. The second transition occurs as the normal displacement limit takes precedence over the shear displacement limit. The third transition occurs as some spines

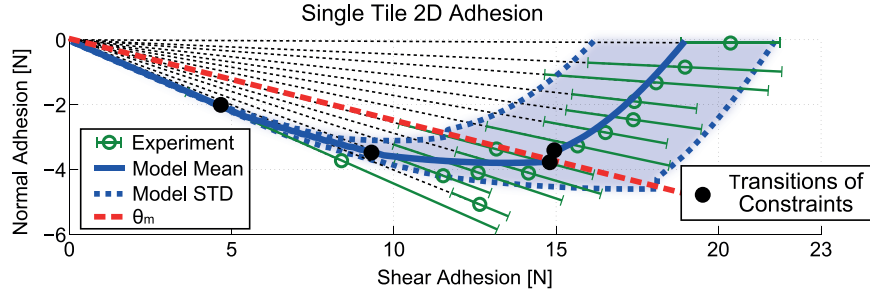


Fig. 12. Experimental verification of the two-dimensional adhesion model. One hundred trials were conducted. Data points represent the average within a 2° angular bin. Error bars indicate one standard deviation for the corresponding force vector. Blue curve represents the expected force from the model and shaded region shows one standard deviation for the model. Marked black dots show transitions among different constraints as discussed in the text.

start to exceed their individual loading angles, and fail. The fourth transition indicates when all the spines exceed their loading angle limits; from here there is a straight line to the origin in force space. Despite the variability, especially at high loading angles, the predictions from the model closely match the measured average forces over a range of angles.

We have not addressed loading in the lateral (y) direction. The spine tile is not designed to support loads in this direction and supports only small loads before slipping. To support lateral loads, a solution is to combine multiple, opposed pairs of spine tiles, arranged in different orientations about the z -axis. A similar approach has been presented for directional adhesive tiles on smooth surfaces (Hawkes et al., 2015).

3.3. Design parameter tuning

Using the stochastic adhesion model from the previous section, we can explore the effects of adjusting different design parameters. In the following paragraphs, we examine the effects of varying the unit length d_{unit} , the stroke, d_{stroke} , and maximum force, F_{max} , when a spine just reaches its full stroke. Note that F_{max} is different from F_{limit} , where F_{max} is the spine force right at the end of the stroke without overloading the spines and is a design parameter, and F_{limit} is the true limit of a spine force before breaking the spine/asperity and is an intrinsic property of the spine/asperity. On different asperities, F_{max} can be either larger or smaller than F_{limit} . For the stroke parameter, we only discuss the shear stroke for shear loading here because in most applications the loading is restricted to below θ_m , and the normal loading can be inferred from shear loading based on the analysis in Section 2. Note also that d_{stroke} and F_{max} determine the spine stiffness: $K = F_{max}/d_{stroke}$. When adjusting one parameter, we fix the other two at moderate values.

3.3.1. Unit length tuning. As noted in Section 2.1, decreasing d_{unit} has a filtering effect such that only asperities with slopes that can sustain some normal load will be engaged during the preload process. According to Asbeck et al. (2006), the number of usable asperities decreases

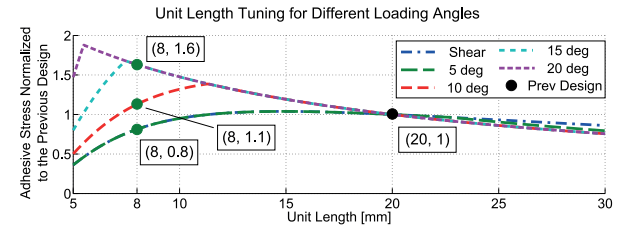


Fig. 13. Effects of varying d_{unit} : maximum forces at different loading angles are normalized, compared with the previous climbing design (Asbeck et al., 2006) ($d_{unit} = 20$ mm). Taking $d_{unit} = 8$ mm is a compromise with good performance at high loading angles ($\phi > 15^\circ$) and reasonable performance in shear.

almost linearly as the asperity slope increases. As a result, a spine with a shorter d_{unit} can catch fewer asperities, but all the asperities it catches can provide a substantial loading angle. For simplicity of comparison, we assume that the spine/asperity contact strength is constant for various unit lengths and loading angles. Referring to Figure 13, we can compare new designs to the previous design in Asbeck and Cutkosky (2012). Let the original case with $d_{unit} = 20$ mm have a normalized maximum force of 1. At low loading angles, it is desirable to maintain the original design with a long unit length to catch as many asperities as possible. In fact, we observe there is a range of lengths from 10 to 25 mm for which the force is nearly the same. At higher loading angles, a shorter d_{unit} is advantageous as only steep asperities can be caught. With shorter d_{unit} we can also have more spines per unit area, which increases the maximum adhesive stress. Cusps, most visible in the curves for 15° and 20°, mark the transition from cases where (i) for short d_{unit} any asperity that a spine catches during preload will also sustain the pulling load to cases (ii) where this is no longer true. Given the results of Figure 13, we chose $d_{unit} = 8$ mm as a compromise that performs well over a range of loading angles for further analysis. Note that longer unit length (e.g. 20 mm) also contributes to larger normal travel, which can be more adaptive to bumpy and irregular surfaces.

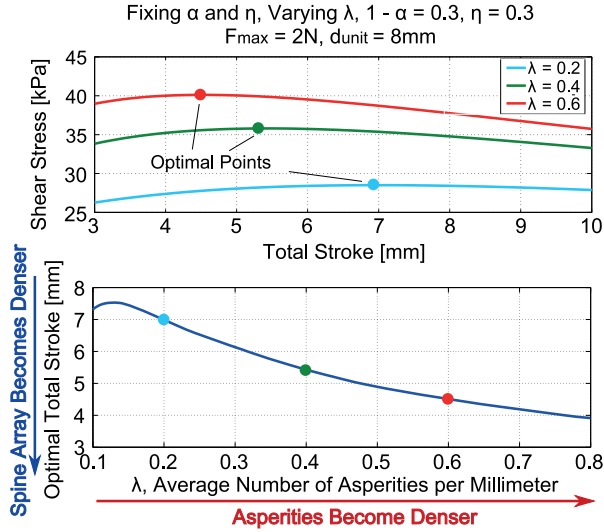


Fig. 14. Effects of varying the stroke length with other parameters fixed. Top: Maximum adhesive stress for different values of maximum stroke and different asperity densities. Bottom: The optimal choice of d_{stroke} becomes shorter as asperity density increases. For small λ the asperity density is more dependent on α , and the detailed trend is shown in Appendix D.

3.3.2. Total stroke tuning. Figure 14 shows the effect of varying the stroke length. With a fixed unit length and maximum single-spine force, a longer stroke corresponds to a lower stiffness, which contributes to better load-sharing among spines. However, a longer stroke reduces the number of spines per unit area of the tile, which decreases the maximum stress. Figure 14 shows the trend of the optimal stroke versus different asperity densities for $0.1 \leq \lambda \leq 0.8$ while fixing $1 - \alpha = 0.3$ and $\eta = 0.3$. The maximum single spine force and the spine unit length are fixed at 2 N and 8 mm respectively. As asperity density increases, it is desirable to have a smaller stroke to create a denser spine array. Assuming a fixed maximum single spine force, spine stiffness increases as well. However, if a surface has sparsely distributed asperities, it is preferable to have soft spines with longer travel for better load-sharing. A more thorough analysis is presented in Appendix D, where all three surface parameters are varied.

3.3.3. Maximum single spine force. Given the same unit length and total stroke, the spine density on a tile is fixed, and thus the total adhesion is dependent on the adhesive capability of each spine. This is a function of the asperity strength distribution. A low maximum spine force, F_{max} , leads to a small overall adhesion but prevents asperity failures; a high maximum spine force contributes to a possibly large load capability but may constantly cause asperity failures. Varying the maximum spine force with d_{unit} and d_{stroke} fixed is accomplished by varying the spine flexure stiffness. Figure 15 shows the trend of the optimal choice of the maximum single spine force versus asperity strength

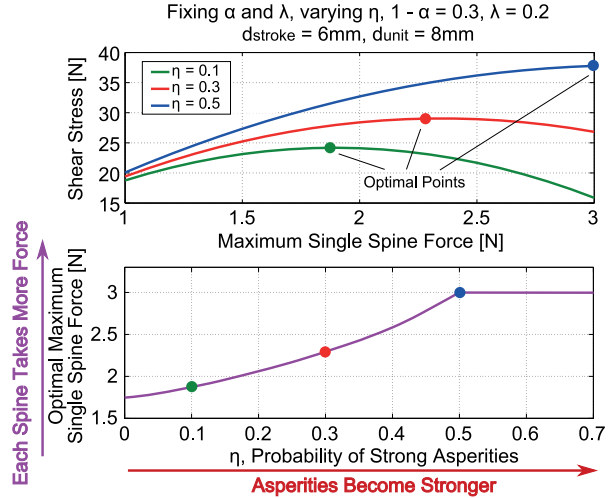


Fig. 15. Tuning the maximum single spine force: maximum shear stress increases with maximum single spine force (or stiffness) as asperities become stronger. It is preferred to have each spine take a high force if strong asperities have a high probability of occurrence.

distributions indicated by η . The upper two curves correspond approximately to the characteristics of concrete and roofing shingle in Figure 4. The asperity spatial distribution is fixed with $1 - \alpha = 0.3$ and $\lambda = 0.2$. The total stroke and unit length are fixed at 6 and 8 mm, respectively. The maximum spine force is limited to 3 N to protect the microspines from damage. The lower plot shows that as asperities become stronger, it is desirable to have stiffer spines and to let each spine take more force. A more detailed analysis with variations in all three surface parameters is given in Appendix D.

4. Opposed-direction spine mechanism

Unidirectional spine tiles can support a load primarily parallel to a surface, with a small force component away from it. To sustain forces primarily in the normal direction a solution is to use opposed pairs of spine tiles, with an internal grasping force parallel to the surface. The magnitude of the internal force, the stiffness of the mechanism, and the displacement limits all determine the overall force capabilities of the opposed spine mechanism.

4.1. Mechanism design

In a basic opposed-spine mechanism (Figure 16), two spine tiles are constrained on a rail. In use, the two tiles are first pulled apart toward their outer hard stops. The mechanism is then placed against a surface and a spring pulls the tiles inward, achieving a grasp. Different rows of spines on a tile engage differently on asperities due to the surface stochastic nature. The moment caused by such uneven engagement is balanced by the rail and the opposite tile; the tiles are far

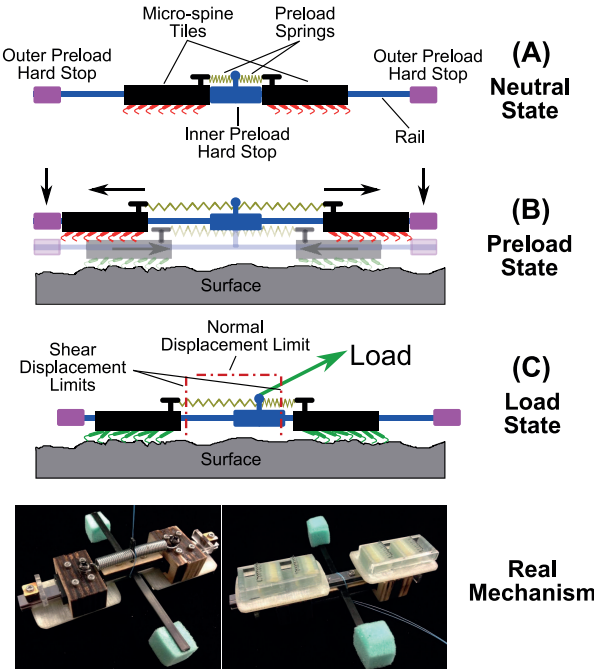


Fig. 16. Schematic and images of the opposed-spine mechanism. Inner and outer hard stops define the range of motion of tiles during preload. Shear and normal displacement limits define the range of motion when loaded.

enough apart that this moment has little effect on the overall adhesion of the unit, and we ignore it in the following analysis.

Applying a load with a tangential component causes the rail to move horizontally (Figure 16(C)) by an amount that depends on the stiffness of the springs and the spines. As in the two-dimensional loading analysis in Section 3, we impose displacement limits in the shear and normal directions to prevent overloading. To release the gripper, the tiles are pulled apart using a cam or similar mechanism.

4.2. Modeling of opposed micro-spines

4.2.1. Simple two-spine model To understand the behavior we start with just two opposed spines (Figure 17). Each spine has a flexure with a tendon attached for applying the loading force. The tendons join at the center, where the external load is applied. Figure 17 shows the arrangement for the case of an external load, F_{ext} , applied mostly in the normal direction.

The opposed spines are preloaded in shear before applying external loads through the middle point. As before, each spine can only be loaded within certain angle and absolute force limits constrained by the asperities. Based on the loading angle and force constraints of each spine, the load capability in any loading direction can be calculated as follows:

$$\begin{cases} F_{ext_s} = F_{s1} - F_{s2} \\ F_{ext_n} = F_{n1} + F_{n2} \end{cases} \quad (6)$$

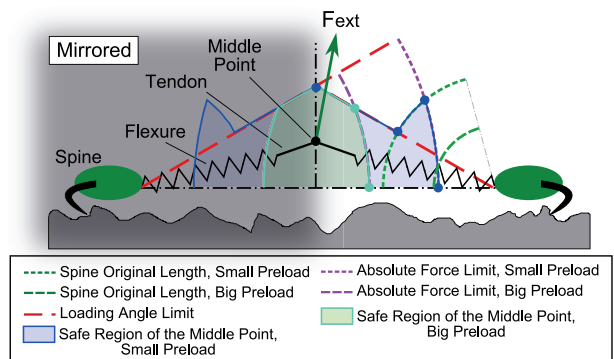


Fig. 17. Diagram of a pair of opposed spines and the corresponding safe loading regions of the middle point.

$$\begin{cases} \sqrt{F_{s1}^2 + F_{n1}^2} < F_{limit} \\ \sqrt{F_{s2}^2 + F_{n2}^2} < F_{limit} \end{cases} \quad (7)$$

$$\begin{cases} \arctan \frac{F_{n1}}{F_{s1}} < \theta_{th} \\ \arctan \frac{F_{n2}}{F_{s2}} < \theta_{th} \end{cases} \quad (8)$$

where F_{ext_s} and F_{ext_n} are the shear and normal external forces; F_{s1} and F_{n1} are the shear and normal forces of the left spine; and F_{s2} and F_{n2} are the shear and normal forces of the right spine.

If loading conditions are such that a spine remains in contact with the surface but experiences no force, this is not considered a failure. As seen in Figure 17, when the external load is oriented, for example, towards the right, the safe region of the middle point is affected by the loading angle limits of the spines, the absolute force limit of the left spine, and the total original lengths of the right spine, flexure, and tendon. With different level of preload, the loads of the two spines are constrained by different force and angular limits. There are all together four constraint scenarios, but for simplicity, we only explain two of them.

With a small preload, the middle loading point can move a large distance before the left spine reaches its force limit, possibly causing the right spine to have no force (in which case it is not constrained by angle or loading limits). The resulting safe region of the middle point is denoted as the blue shaded region, and the boundary of this region is shown with a solid blue line. The analysis for loading to the left is symmetric. With a large preload, the middle point cannot move much before the left spine reaches its force limit. The right spine always has a load in this case. The corresponding safe region of the middle point is shown with a light green shaded area. Interestingly, although the safe region of the middle point is smaller for the case of a high preload, we will see in the next section that a high preload is usually preferable for grasping with arrays of opposed spines.

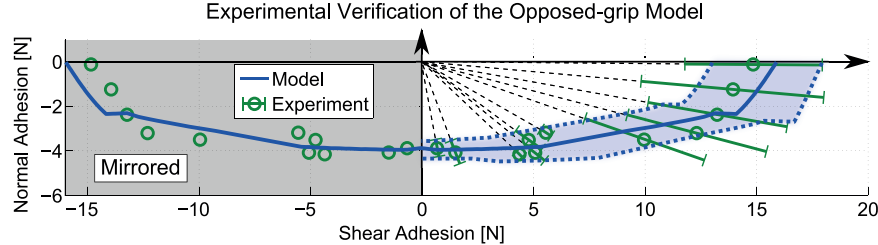


Fig. 18. Experimental verification of opposed spine-tile model on a fine concrete surface for 100 data points within every 5° . Blue shaded region shows one standard deviation of the expected adhesion in the model. The left side of the plot is mirrored.

4.2.2. Opposed spine tiles The above analysis is a simplified opposed-spine model. In real uses, the individual spines on a tile engage with the asperities differently during preload and can provide different adhesion during loading. However, each spine is still constrained by its own loading angle limit and absolute force limit based on the design parameters and asperity distributions.

The behavior of opposed spine tiles follows the same general pattern as the simplified two-spine model. As in Section 3, we use a stochastic model for the expected force available from each tile as a function of loading angle and surface properties. To protect the spines, as in Section 3, we impose displacement limits on the mechanism in the shear and normal directions. The detailed calculation is provided in Appendix E. Referring to Figure 16, the preload springs are in series with spines and their flexures, and therefore reduce the overall spine stiffness. As seen in the next section, this has a significant effect on overall force capacity.

Experiments were conducted on a fine concrete surface to verify the model. The opposed spine mechanisms had 20 spines on each tile with the following parameters: $d_{unit} = 8$ mm, $F_{max} = 2$ N, and $d_{stroke} = 6$ mm. The preload spring in the middle has a stiffness of $K_m = 1$ N/mm and an initial force of 6.6 N with the mechanism at the neutral state. The total preload distance is 6 mm. The shear limit is placed at the full stroke of the tile and the normal limit 1.3 mm above the surface. One hundred data points were recorded with various loading orientations from pure shear to pure normal. With the assumption that the surface is isotropic, and the two sides of the mechanism are almost identical, we take data only for loads to one side and mirror the results. The comparison between the model and the experiments is shown in Figure 18.

Each illustrated point is the average of the data within a 5° angular range. The error bars indicate one standard deviation. The blue solid line shows the modeled mean adhesion, and the blue shaded region indicates one standard deviation in the model. Note that the adhesion variance for loads primarily in the normal direction is relatively small. Given the mechanism design and preload, small variations in load angle around the normal have little effect on the load experienced by each spine. On the right side, proceeding in clockwise direction, the first sharp turn in the blue curve

is the transition between the normal limit and shear limit becoming active; the second turn is the transition from the right tile having some force to no force.

4.3. Mechanism tuning

With the experimentally verified model, we can tune the mechanism parameters for a better adhesive capability. Spine parameter tuning has been presented in Section 3.3; here we focus on opposed mechanism parameters including the stiffness and initial force of the middle spring.

4.3.1. Mechanism preload. A small preload leads to fewer engaged spines in each tile and a lower force in most directions except pure shear, where unengaged spines can still catch asperities during loading. With a large preload, more spines engage asperities before the external load is applied, resulting in a larger available force, especially in the normal direction. However, a large preload also means that much of the available shear force from each tile is canceled by the opposite tile. Hence, the available force parallel to the surface may be less.

Figure 19 shows the effects of varying the spring stretch and corresponding gripping force for a stiff system on a concrete surface. Note that one can use a toggle mechanism, as in the example shown in Section 5, for assistance when the stretching force is large. In the simulation, we set $d_{unit} = 8$ mm, $d_{stroke} = 6$ mm, and $F_{max} = 2$ N. Each tile again contains 20 spines. The middle spring in this case is quite stiff, $K_m = 100$ N/mm, so that the stiffness after gripping is determined in practice by the spines and their flexures, which have a stiffness of roughly 3 N/mm per tile, depending on how many spines are engaged. As in previous examples, the shear limit is set to 6 mm and the normal limit to 1.3 mm. The middle spring starts at its rest length and is stretched by varying amounts prior to bringing the tiles in contact with the surface. In this case, we see that the highest normal stress is possible with the largest stretch but at the expense of a maximum shear stress that is only one-half of the other cases.

4.3.2. Preload spring stiffness Figure 20 illustrates the effect of varying the mechanism middle spring stiffness in

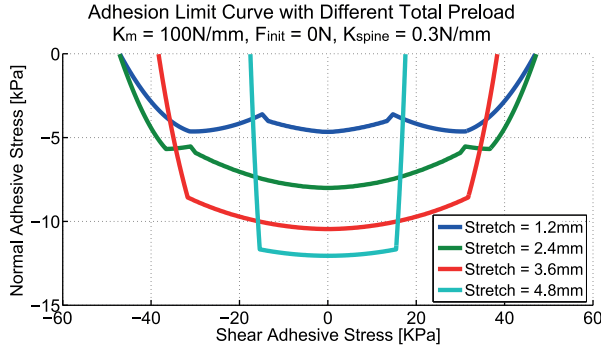


Fig. 19. Simulated adhesive stress limit curves for different total preload distances on fine concrete surfaces. A larger stretch, and correspondingly larger initial gripping force, leads to larger maximum normal stress but less shear.

combination with any initial bias force that must be overcome to start forcing the tiles apart. The spine and mechanism parameters used in the simulation are the same as in Figure 19. The best results are obtained with either a stiff spring and little or no initial force ($K_m = 100 \text{ N/mm}$, $F_{init} = 0$) or with a relatively soft spring and substantial initial force ($K_m = 0.5 \text{ N/mm}$, $F_{init} = 18 \text{ N}$), such that for most loads the middle spring is effectively rigid. In the former case, the mechanism spring is again in series with the spines and flexures, so the actual stiffness after gripping is considerably lower. The latter case approximates a constant-force spring and requires less effort to pull the tiles apart for gripping. The middle spring initial force should be chosen so that the gripping force is not excessive on weak surfaces. On strong surfaces the forces from the spines will overcome the middle spring initial force and ultimately cause the mechanism to reach a hard stop. The hard stop acts like a stiff spring, which makes the spring transition from the latter case to the former case, ensuring strong grip on strong surfaces as well. With an appropriate choice of the initial force, low spring stiffness, and the hard stop, this solution ensures a relatively consistent force on the spines and becomes the preferred solution.

5. Applications

Large arrays of compliant micro-spines have been used in applications such as human climbing (Asbeck, 2010) and asteroid grappling and drilling (Parness et al., 2013). They can benefit from the insights presented in this paper to achieve high shear and normal stresses in a compact package. A second area of interest is in perching UAVs where forces are comparatively low, but space and weight are at a premium. In this section we describe a gripper that allows a quadrotor to perch on rough walls and ceilings.

Figure 21 shows a gripper adapted from the linear opposed-spine mechanism in Figure 16. As in the previously described mechanism, there are two tiles with spines that travel along linear rails. The spine unit length is 20

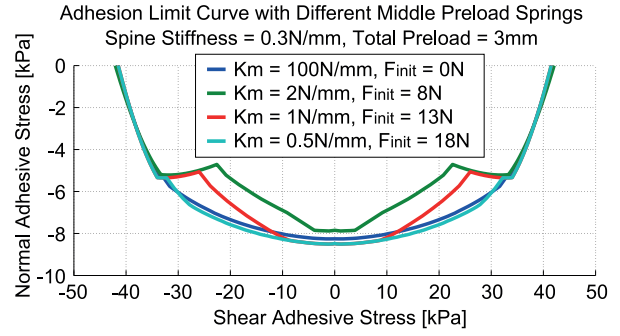


Fig. 20. Computed adhesive stress limit curves for different middle spring stiffnesses and initial force values, which produce initial forces, F_{init} , that must be overcome to pull the tiles apart. Largest loads are possible with either a stiff middle spring or a soft spring and a substantial initial force, which approximates the case of a constant-force spring.

mm to increase the travel in the surface normal direction, which makes the mechanism better adapt to irregular surfaces and misalignment at first contact in the cases of non-ideal flight control. However, as discussed in the Section 3.3, this design choice also makes the mechanism less compact than it could be. In the neutral, unloaded state, the truss points upward and a reset spring pulls the spines toward their starting position. As the quadrotor contacts a wall or ceiling, it applies a force that depresses the top of the truss mechanism. As it collapses, the truss pulls a tendon that forces the tiles apart, stretching preload springs that provide the gripping force. The truss creates an over-center mechanism so that when fully depressed it contacts a hard stop and remains stably in the collapsed position (engaged state) with a preload applied to the spines. Loads are exerted directly on the frame of the mechanism through a loading tendon that is routed around the truss for two cycles. This arrangement eliminates slack that is otherwise caused by the unequal travels of the apex of the truss and the two ends of the truss. To release the gripper, a small force on the release tendon (shown in red) suffices to pop the truss out of its over-center configuration.

Experiments were conducted with a 150 g RC quadrotor with a 15 g opposed micro-spine gripper mounted overhead. The gripper has eight spines on each side. An additional group of three spines is located at the end of a “tail” used for perching on walls. The quadrotor flies tail-first into a wall and pitches upward, so that the gripper comes in contact with the wall. The rotors continue to spin until the truss mechanism collapses and the gripper attaches to the wall, as seen in the multiple-exposure image in Figure 22. Once perched, the gripper supplies the necessary force to prevent the quadrotor from pitching backward. The tail spines provide the shear force needed to counteract gravity along the wall. For release, a small servo pops the collapsed truss open and the quadrotor pitches backward, around the still-engaged tail spines. After a short delay, the rotors spin up

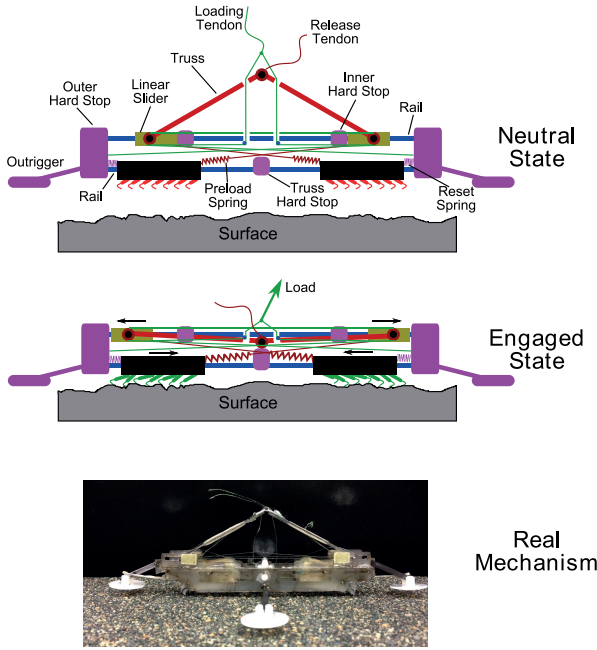


Fig. 21. Diagrams and photograph of the opposed perching gripper ($d_{unit} = 20$ mm, $d_{stroke} = 10$ mm, $F_{max} = 2$ N, $K_m = 2$ N/mm, $F_{init} = 5$ N). The preload spring bottoms out after a 3 mm stretch.

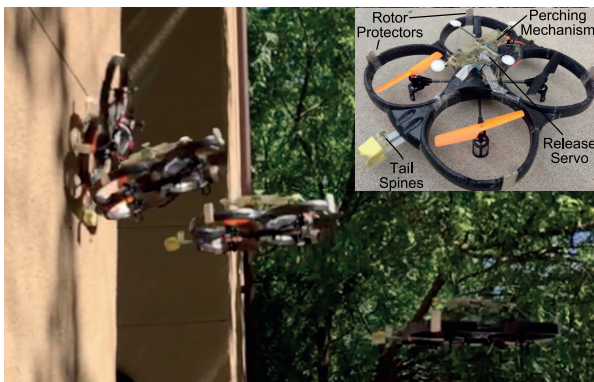


Fig. 22. The flight sequence of a quadrotor perching on a vertical rough surface. The quadrotor pivots forward on its tail spines to align with the surface and collapse the truss mechanism.

to resume flight. For inverted surface perching, the quadrotor flies directly into a ceiling surface to collapse the truss. Again, the quadrotor detaches from the surface by releasing the truss and, after a short delay, spinning the rotors to resume flight. The average perching success rate on stucco and concrete surfaces is approximately 70% for both vertical and overhanging surfaces. On vertical surfaces, the required adhesion force is lower, however the quadrotor is more sensitive to alignment errors as it pitches up around its tail. The quadrotor is also typically more exposed to wind gusts on walls than on ceilings. On ceilings the main cause of failure is a surface without sufficient asperities to achieve a strong grip.

6. Conclusion

We have presented detailed models of compliant spines that engage asperities on rough surfaces. The distribution of asperities and the spine/asperity contact strength are stochastic, which leads to probabilistic models of the expected force from an array of compliantly supported spines. The spine-to-spine variation is large, but the predicted average force values match empirical results. The models also permit one to explore the effects of parametric design variations in spine flexure length, stiffness, etc. In particular, for opposed-spine grippers, the models lead to a new design with a short unit length to pack more spines in a unit area and relatively high stiffness in comparison with previous mechanisms used for climbing robots. The new design results in somewhat less load sharing because fewer spines engage and take the external load and each spine carries more force, especially when loads are mostly parallel to the surface. However, it more than makes up for this in increased spine density.

The spine mechanism models are extended to grippers with sets of opposed spines that can sustain substantial loads perpendicular to a surface, e.g. to cling to a ceiling. Again, the models permit one to explore variations in design parameters including the spring stiffness and preload for the gripping mechanism. Experiments with opposed spine mechanisms confirm the predicted behavior. Tuned design parameters enable climbing robots to hold on to rough surfaces more stably and aerial robots to perch on outdoor building surfaces with smaller grippers than using previous spine designs. As a demonstration, we tested an opposed micro-spine mechanism on an RC quadrotor that perches outdoors, on vertical and inverted rough surfaces.

Because spine/asperity engagement is inherently probabilistic, with considerable variation, the models and designs presented here should be combined with force sensing for reliable performance in applications. Fortunately, it is the case that if a spine/asperity contact is going to fail, it often fails early, at a relatively small fraction of the expected force. Therefore, climbing robots with force sensors can adopt a “grip and test” strategy, applying a fraction of the expected load before trusting the grip. For a perching quadrotor, it is straightforward to tell whether the gripper has caught on asperities by checking that the internal spring remains stretched. In addition, the on-board accelerometers will indicate whether it is falling, in which case the rotors can be spun up to resume flight. Future work also involves taking load redistribution when spines fail into consideration for higher modeling accuracy.

Acknowledgements

We thank Morgan Pope and Will Roderick for their help with the quadrotor perching experiments. We thank Elliot Hawkes, Eric Eason, and Capella Kerst for their help with spine adhesion measurements.

Funding

This work was supported by the NSF (grant number IIS-1161679) and ARL (grant number MAST MCE 15-4).

ORCID iDs

Hao Jiang,  <http://orcid.org/0000-0003-4477-529X>
Shiquan Wang,  <http://orcid.org/0000-0003-3245-4579>

References

- Asbeck AT (2010) *Compliant Directional Suspensions for Climbing with Spines and Adhesives*. PhD Thesis, Stanford University.
- Asbeck AT and Cutkosky MR (2012) Designing compliant spine mechanisms for climbing. *Journal of Mechanisms and Robotics* 4(3): 031007.
- Asbeck AT, Kim S, Cutkosky MR, Provancher WR and Lanzetta M (2006) Scaling hard vertical surfaces with compliant microspine arrays. *The International Journal of Robotics Research* 25(12): 1165–1179.
- Dai Z, Gorb SN and Schwarz U (2002) Roughness-dependent friction force of the tarsal claw system in the beetle *Pachnoda marginata* (coleoptera, scarabaeidae). *Journal of Experimental Biology* 205(16): 2479–2488.
- Dalton KA, Wei TE, Horchler AD, Southard L, Wile GD, Quinn RD, Gorb SN and Ritzmann RE (2009) Mini-whegs tm climbs steep surfaces using insect-inspired attachment mechanisms. *The International Journal of Robotics Research* 28(2): 285–302.
- Desbiens AL, Asbeck AT and Cutkosky MR (2011) Landing, perching and taking off from vertical surfaces. *The International Journal of Robotics Research* 30(3): 355–370.
- Hawkes EW, Jiang H and Cutkosky MR (2015) Three-dimensional dynamic surface grasping with dry adhesion. *The International Journal of Robotics Research* 35(8): 943–958.
- Jiang H, Pope MT, Hawkes EW, et al. (2014) Modeling the dynamics of perching with opposed-grip mechanisms. In: *2014 IEEE International Conference on Robotics and Automation (ICRA)*. IEEE, pp. 3102–3108.
- Kovac M, Germann JM, Hurzeler C, Siegwart R and Floreano D (2009) A perching mechanism for micro aerial vehicles. *Journal of Micro-Nano Mechatronics* 5: 77–91.
- Lam TL and Xu Y (2012) Biologically inspired tree-climbing robot with continuum maneuvering mechanism. *Journal of Field Robotics* 29(6): 843–860.
- Lee JS and Fearing RS (2015) Anisotropic collapsible leg spines for increased millirobot traction. In: *2015 IEEE International Conference on Robotics and Automation (ICRA)*. IEEE, pp. 4547–4553.
- Liu Y, Sun S, Wu X and Mei T (2015) A wheeled wall-climbing robot with bio-inspired spine mechanisms. *Journal of Bionic Engineering* 12(1): 17–28.
- Lynch GA, Clark JE, Lin PC and Koditschek DE (2012) A bioinspired dynamical vertical climbing robot. *The International Journal of Robotics Research* 31(8): 974–996.
- Momber A (2004) Damage to rocks and cementitious materials from solid impact. *Rock Mechanics and Rock Engineering* 37(1): 57–82.
- Parness A (2011) Anchoring foot mechanisms for sampling and mobility in microgravity. In: *2011 IEEE International Conference on Robotics and Automation (ICRA)*. IEEE, pp. 6596–6599.
- Parness A, Carpenter KC and Wiltsie N (2015) Terrain traversing device having a wheel with microhooks. US Patent 8,978,807.
- Parness A, Frost M, Thatte N, et al. (2013) Gravity-independent rock-climbing robot and a sample acquisition tool with microspine grippers. *Journal of Field Robotics* 30(6): 897–915.
- Pope MT and Cutkosky MR (2016) Thrust-assisted perching and climbing for a bioinspired UAV. In: *Conference on Biomimetic and Biohybrid Systems*. New York: Springer, pp. 288–296.
- Pope MT, Kimes CW, Jiang H, et al. (2017) A multimodal robot for perching and climbing on vertical outdoor surfaces. *IEEE Transactions on Robotics* 33(1): 38–48.
- Roderick WR, Cutkosky MR and Lentink D (2017) Touchdown to take-off: at the interface of flight and surface locomotion. *Interface Focus* 7(1): 20160094.
- Sintov A, Avramovich T and Shapiro A (2011) Design and motion planning of an autonomous climbing robot with claws. *Robotics and Autonomous Systems* 59(11): 1008–1019.
- Spenko M, Haynes GC, Saunders J, et al. (2008) Biologically inspired climbing with a hexapedal robot. *Journal of Field Robotics* 25(4–5): 223–242.
- Wang S, Jiang H and Cutkosky MR (2016) A palm for a rock climbing robot based on dense arrays of micro-spines. In: *2016 IEEE/RSJ International Conference on Intelligent Robots and Systems (IROS)*. IEEE, pp. 52–59.
- Xu F, Wang B, Shen J, Hu J and Jiang G (2017) Design and realization of the claw gripper system of a climbing robot. *Journal of Intelligent and Robotic Systems* 89(3–4): 301–317.

Appendix A. Derivation of a micro-spine's travel following an exponential distribution

As shown in Figure 23, for an arbitrary starting point on a surface, the distance between this point and the previous asperity is t , and the distance between this point and the next asperity is s . Let X be the random variable of the interval distance between adjacent asperities, then the probability of this situation happening is

$$\Pr(X = t + s \mid X \geq t) = \frac{\Pr(X = t + s, X \geq t)}{\Pr(X \geq t)} \quad (9)$$

$$= \begin{cases} 0 & \text{if } s < 0 \\ \Pr(X = t + s) & \text{if } s \geq 0 \\ \Pr(X \geq t) & \end{cases} \quad (10)$$

$$= \begin{cases} 0 & \text{if } s < 0 \\ \lambda e^{-\lambda(t+s)} & \text{if } s \geq 0 \\ \int_t^\infty \lambda e^{-\lambda x} dx & \end{cases} \quad (11)$$

$$= \begin{cases} 0 & \text{if } s < 0 \\ \lambda e^{-\lambda(t+s)} & \text{if } s \geq 0 \\ e^{-\lambda t} & \end{cases} \quad (12)$$

$$= \begin{cases} 0 & \text{if } s < 0 \\ \lambda e^{-\lambda s} & \text{if } s \geq 0 \\ \lambda e^{-\lambda s} & \end{cases} \quad (13)$$

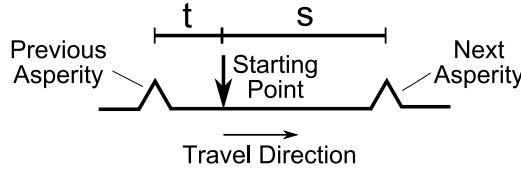


Fig. 23. Schematic of a spine starts at a random point to travel on a surface.

Thus, the probability density of the distance between this point and the next asperity equaling to s is the same exponential distribution function as the asperity interval distance. Note that t and s can be interchanged, and thus the distance between this point and the previous asperity also follows the same exponential distribution as the asperity interval distance. This can also be viewed as the distance between this point and the next asperity if the spine is dragged in the opposite direction, which explains the isotropic properties of spine/asperity engagement on surfaces.

Appendix B. Justification of sample size selection in asperity distribution characterizations

In both asperity spatial and strength distributions the number of trials for each surface is 150. At this sample size, the parameters of the distributions stabilize and the RMS error decreases to a low level. Figures 24 and 25 show the convergence for the asperity spatial and strength distributions, respectively. For the strength cumulative distribution data, darker lines correspond to larger sample sizes.

Appendix C. Single-tile two-dimensional adhesion modeling details

The shear and normal adhesion of a spine tile can be derived from each spine's force and loading angle. During preloading, all the spines are dragged in shear and the model from Section 3 applies directly. Subsequently, spines are loaded away from the surface. For small loading angles (e.g. 5° or less), the spines remain in contact with the surface enough to re-engage. For larger angles (e.g. 15°) they depart the surface and cannot further engage or re-engage. Thus, we should compare the travel of the tile in the direction away from the surface with the average asperity height or depth. To simplify the calculation we take the average tile normal stroke (half the normal stroke) and compare it with the average asperity height or depth. The calculation proceeds as follows:

$$\begin{aligned} F_{ext_s} = & N \int_0^L p(\alpha, \lambda; x) F(D, x) \cos \phi(x) Pr(F) dx \\ & + 1\{H \leq 2h_a\} \int_0^D \frac{2h_a - H}{2h_a} p(\alpha, \lambda; z + L) \\ & F'(D, z) \cos \phi'(z) Pr(F') dz \end{aligned} \quad (14)$$

$$\begin{aligned} F_{ext_n} = & N \int_0^L p(\alpha, \lambda; x) F(D, x) \sin \phi(x) Pr(F) dx \\ & + 1\{H \leq 2h_a\} \int_0^D \frac{2h_a - H}{2h_a} p(\alpha, \lambda; z + L) \\ & F'(D, z) \sin \phi'(z) Pr(F') dz \end{aligned} \quad (15)$$

where

$$\begin{cases} F(D, x) = K(\sqrt{(L + L_o - x + D)^2 + H^2} - L_o) \\ F'(D, z) = K(\sqrt{(D - z + L_o)^2 + H^2} - L_o) \end{cases} \quad (16)$$

and

$$\begin{cases} \phi(x) = \arctan \frac{H}{L_o + L - x + D} \\ \phi'(z) = \arctan \frac{H}{L_o + D - z} \end{cases} \quad (17)$$

$$D = D_{limit} \quad \text{or} \quad H = H_{limit} \quad (18)$$

In the foregoing expressions, and with reference to Figure 11, F_{ext} is the external load, L is the shear preload distance, ϕ and ϕ' are the loading angles of single spines, depending on whether a spine can further engage with asperities after preload, F and F' are individual spine forces, with or without further engagement after preload, L_o is the original length of the spine, D and H are the actual tile stroke in shear and normal in the loading state, corresponding to the external loading angle, h_a is the average depth/height of asperities, and D_{limit} and H_{limit} are the allowed maximum stroke in shear and normal directions, bounded by displacement limits. At full stroke for any loading angle, either D reaches D_{limit} or H reaches H_{limit} . If $\phi(x)$ or $\phi'(z)$ exceeds the empirical loading angle limit θ_{th} , the corresponding $F(D, x)$ or $F'(D, z)$ is zero.

Appendix D. Design parameter tuning for three surface properties

A more thorough tuning of spine total stroke than in Section 3 is shown in Figure 26, where all three surface parameters are varied. This parameter tuning applies to both one- and two-dimensional loading because the unit length is fixed, and thus the number of usable asperities does not change with stroke. The optimal choice of stroke is mainly affected by $1 - \alpha$ and λ , indicating asperity spatial distributions. Although the total adhesion of a spine tile is affected by the asperity strength distribution, the optimal choice of stroke is not sensitive to it.

A more detailed tuning of single spine maximum force than in Section 3 is shown in Figure 27. All three surface parameters are varied. This parameter tuning also applies to both one- and two-dimensional loading with the unit length fixed. In contrast to spine stroke tuning, the optimal choice of the maximum spine force is mainly affected by the asperity strength distribution. Asperity spatial distribution has little effect on the choice of the maximum spine force.

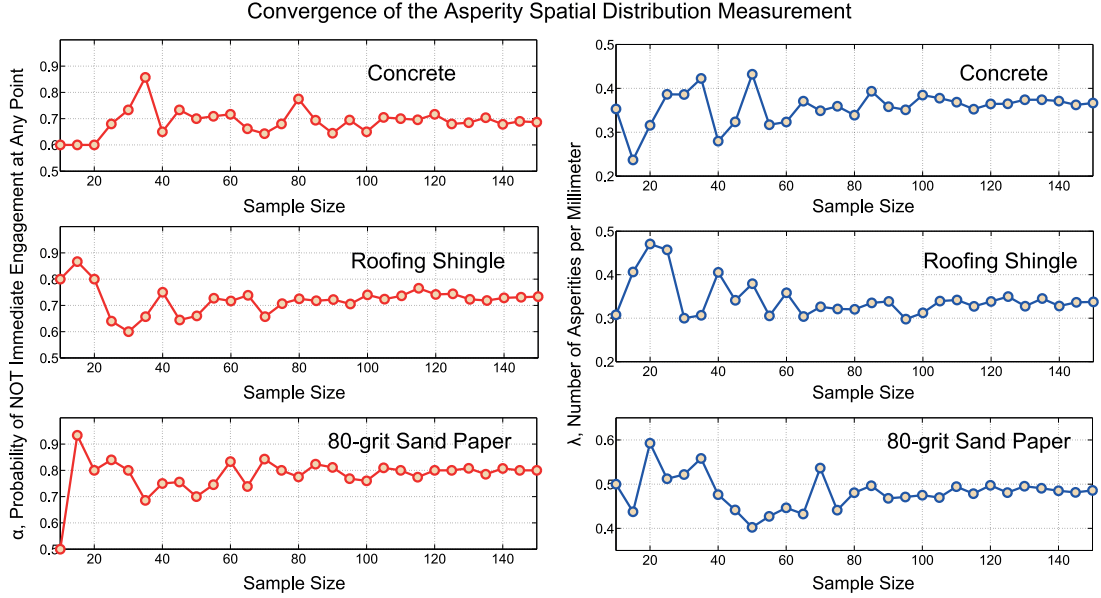


Fig. 24. Convergence of parameters describing asperity spatial distribution as sample size increases.

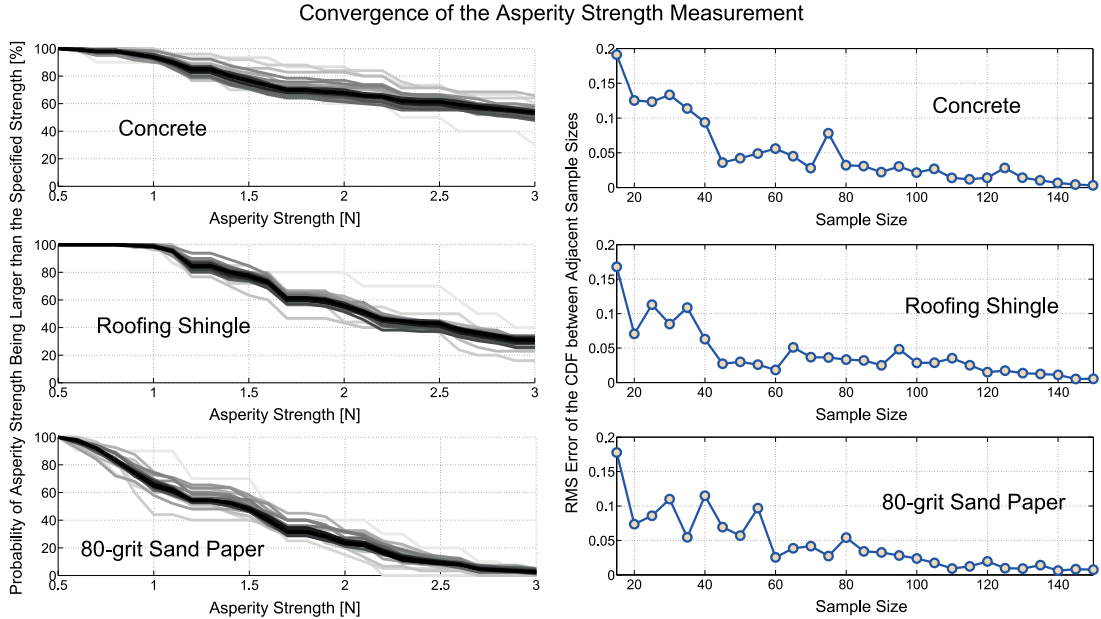


Fig. 25. Convergence of asperity strength cumulative distribution as sample size increases. Darker lines correspond to larger sample sizes. All the lines have the same line width. The RMS error of the raw data also decreases and stabilizes.

Appendix E. Opposed spine mechanism two-dimensional adhesion modeling

The shear forces of the two tiles and the middle spring can be calculated based on the travel of the loading point and the two tiles, as well as the characteristics of the middle spring:

$$F_{preload} = N \int_0^L p(\alpha, \lambda; x) F_{12}(L, x) Pr(F_{12}) dx = K_m L_m + F_{init} \quad (19)$$

$$F_{s1} = K_m(L_m + D_m - D_1) + F_{init} \quad (20)$$

$$F_{s2} = K_m(L_m - D_m + D_2) + F_{init} \quad (21)$$

and the shear and normal adhesion of the two tiles can be calculated based on the tile travel, spine stiffness, and surface properties:

$$F_{s1} = N \int_0^L p(\alpha, \lambda; x) F_1(D_1, x) \cos \phi(x) Pr(F_1) dx + 1\{H \leq 2h_a\} \int_0^D \frac{2h_a - H}{2h_a} p(\alpha, \lambda; z + L) F'_1(D_1, z) \cos \phi'(z) Pr(F'_1) dz \quad (22)$$

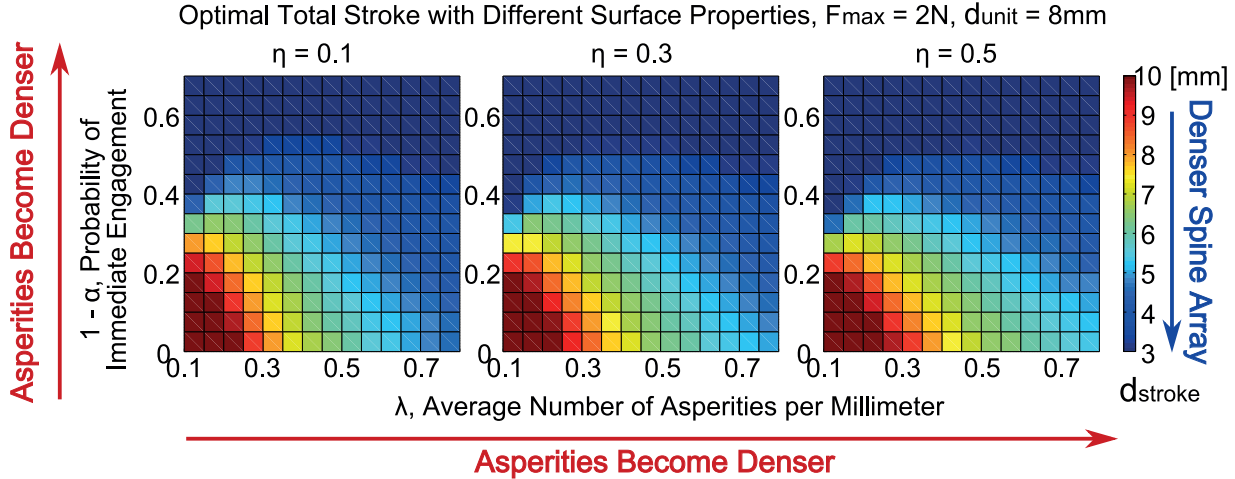


Fig. 26. The complete tuning of spine/tile stroke length over different surface properties. All three surface parameters are varied. The optimal stroke is affected little by the asperity strength distribution.

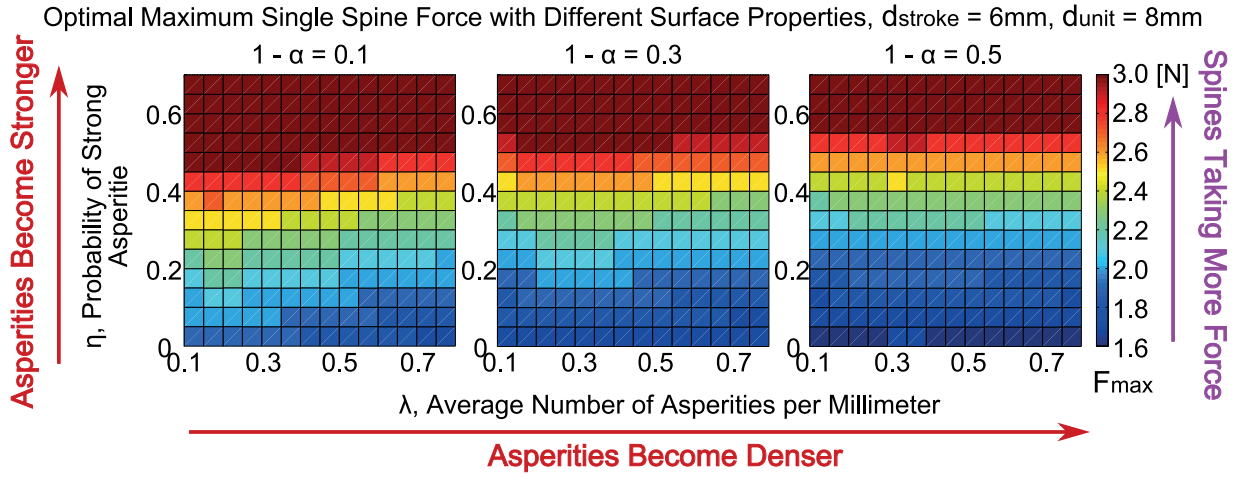


Fig. 27. The complete tuning of the maximum single spine force over different surfaces. All three surface parameters are varied. The optimal maximum spine force is affected little by the asperity spatial distribution.

$$\begin{aligned} F_{n1} = & N \int_0^L p(\alpha, \lambda; x) F_1(D_1, x) \sin \phi(x) Pr(F_1) dx \\ & + \{H \leq 2h_a\} \int_0^D \frac{2h_a - H}{2h_a} p(\alpha, \lambda; z + L) F'_1(D_1, z) \\ & \sin \phi'(z) Pr(F'_1) dz \end{aligned} \quad (23)$$

$$F_{s2} = N \int_0^L p(\alpha, \lambda; x) F_2(D_2, x) \cos \phi(x) Pr(F_2) dx \quad (24)$$

$$F_{n2} = N \int_0^L p(\alpha, \lambda; x) F_2(D_2, x) \sin \phi(x) Pr(F_2) dx \quad (25)$$

$$\begin{cases} F_{ext_s} = F_{s1} - F_{s2} \\ F_{ext_n} = F_{n1} + F_{n2} \end{cases} \quad (26)$$

$$L_{total} = L + L_m \quad (27)$$

where $F_{preload}$ is the shear preload imposed by the middle spring, F_{s1} and F_{n1} are the shear and normal adhesion of the left spine tile, and F_{s2} and F_{n2} are the shear and normal adhesion of the right spine tile. The shear and normal

forces of both spine tiles can be calculated the same way as the two-dimensional adhesion analysis in Section 3. Instead of using $F(D, x)$, here we separate it for the two tiles. The total external load is calculated based on the adhesion of the two tiles. Here $F_1(D_1, x)$ is the total load of a single spine on the left with the base traveling D_1 and spine free traveling x before catching any asperity, and $F_2(D_2, x)$ is the total load of a single spine on the right with the base traveling D_2 and spine free traveling x . Similar definitions apply to F'_1 and F'_2 for consideration that in some high loading angle spines can further engage after preload. Similarly, ϕ_1 and ϕ_2 are the actual loading angles of each spine on the left and right, respectively, and $F_{12}(L, x)$ is the shear preload force of a single spine with a preload distance of L and free travel of x . Here K_m is the natural stiffness of the middle spring, L_m is the stretch of the middle spring during shear preloading, F_{init} is the initial force of the middle spring before any extension, and L_{total} is the total preload distance defined by the positions of the inner and outer hard stops and is the sum

of the tile preload distance and middle spring stretch during preloading. The intermediate variables can be calculated as follows. Again, at full stroke for any loading angle, either D_m reaches D_{limit} or H reaches H_{limit} :

$$\begin{cases} F_{12}(L, x) = K(L - x) \\ F_1(D_1, x) = K(\sqrt{(L - x + D_1 + L_o)^2 + H^2} - L_o) \\ F'_1(D_1, z) = K(\sqrt{(D_1 - z + L_o)^2 + H^2} - L_o) \\ F_2(D_2, x) = K(\sqrt{(L - x - D_2 + L_o)^2 + H^2} - L_o) \end{cases} \quad (28)$$

$$\begin{cases} \tan \phi_1(x) = \frac{H}{L - x + L_o + D_1} \\ \tan \phi'_1(z) = \frac{H}{D_1 + L_o - x} \end{cases} \quad (29)$$

$$\begin{cases} \tan \phi_2(x) = \frac{H}{L - x + L_o - D_2} \\ D_m = D_{limit} \quad \text{or} \quad H = H_{limit} \end{cases} \quad (30)$$